Orientation dependent coherent anti-Stokes Raman scattering of cylindrical microparticle with focused lasers

C. H. Raymond Ooi,* W.-L. Ho, and P. Seow

Department of Physics, University of Malaya, 50603 Kuala Lumpur, Malaysia
*Corresponding author: rooi@um.edu.my

We developed a semi-analytical and semi-classical theory for nonlinear scattering of coherent anti-Stokes Raman scattering (CARS) signal from a cylindrical microparticle by paraxial focused laser beams. We study the effects of radius and length of the microparticle, as well as the orientation on the angular distributions of the CARS signal. The waist of the laser beam is found to have a significant effect on the angular distribution. The combination of Gaussian laser beams and cylindrical geometry yields analytical expressions for the orientation factor and the CARS electric field, which permit convenient and efficient computation of the scattering signal versus various physical parameters. © 2013 Optical Society of America

OCIS codes: (190.3970) Microparticle nonlinear optics; (300.6230) Spectroscopy, coherent anti-Stokes Raman scattering; (190.5650) Raman effect; (290.5910) Scattering, stimulated Raman.
http://dx.doi.org/10.1364/JOSAB.30.002427

1. INTRODUCTION

Coherent anti-Stokes Raman scattering (CARS) is a third-order nonlinear optical four-wave mixing phenomenon based on the contributions of the nonlinear part of the induced dipole moment [1]. It is based on Raman scattering process in which each shift of the frequency of the scattered photons from the incident photon frequency corresponds to a particular internal state transition of the scatterer and supplies information on frequency modulations such as vibrational and rotational transitions in molecules [2]. Since the energy levels of a molecule crucially depend on the molecule's composition, the spectrum of Raman shifts provides unique information on the internal energy level structure [3]. Because of its sensitivity to the chemical structure of a molecule, the Raman signal becomes the reporter of the specific structure and hence bears the fingerprints of the molecule [4]. CARS is more sensitive, as the signal is a few orders of magnitude stronger than Raman scattering.

CARS has been a feasible and common tool for molecular spectroscopy in atom and molecule characterization analysis. The strength of CARS lies not only in the enhancement of the weak Raman signal but also in the mitigation of nonresonant background [5,6]. CARS also permits cumulative excitations of multiple vibrational modes by utilizing manipulated laser pulses. In addition, it is noninvasive and label-free probing. To date, coherent Raman spectroscopy, such as CARS, has gained standing in many applications, especially in the areas of imaging, analytical chemistry, combustion processes, and environment monitoring. It is a popular technique applied in the field of nonlinear optical microscopy through high-resolution imaging in the areas of biology and medicine [7–9]. Examination of living cells and organisms based on molecular vibrations is feasible with this technique. An optical imaging modality that merges stimulated Raman excitation and photoacoustic detection has been reported [10,11]. The stimulated Raman photoacoustic waves form images of the tissue volume by using an ultrasonic transducer. CARS is also used for characterization of gaseous properties in combustion reactions. In addition, CARS serves as a convincing apparatus for spectroscopic recognition of molecular species in distant locations, such as standoff recognition of bacterial spores [12,13]. It may be used for distinction of airborne particles such as anthrax spores from their surroundings in future work. Experimental work in bacterial detection has been reported in which single laser shots were used to acquire the CARS spectrum [14], where the hybrid CARS employed consisted of a pair of broadband Raman excitation pulses combined with a time-delayed narrowband probe pulse [14]. Furthermore, CARS was reported for real-time detection in time-resolved CARS owing to its sensitivity in interrogating molecular vibrations and capability of measuring the decoherence time [15]. There are also studies of standoff detection of warfare agents targeting chemicals such as explosives via backward CARS [16,17].

The essence of Raman signal enhancement is the maximization of the quantum coherence between ground vibrational states of $|b\rangle$ and $|c\rangle$. Femtosecond adaptive spectroscopic technique (FAST) CARS is a revolutionized technique of CARS that utilizes the adiabatic fast passage [18] and the avenue of coherently phased ultrashort pulses in clusters to achieve maximal quantum coherence in biomolecules [19]. Figure 1(a) shows the configuration of FAST CARS. It is dissimilar from CARS in the sense that the former embraces the maximization of ground-state molecular quantum coherence. A carefully manipulated set of coherent excitation laser pulses is responsible for creating maximal ground-state coherence
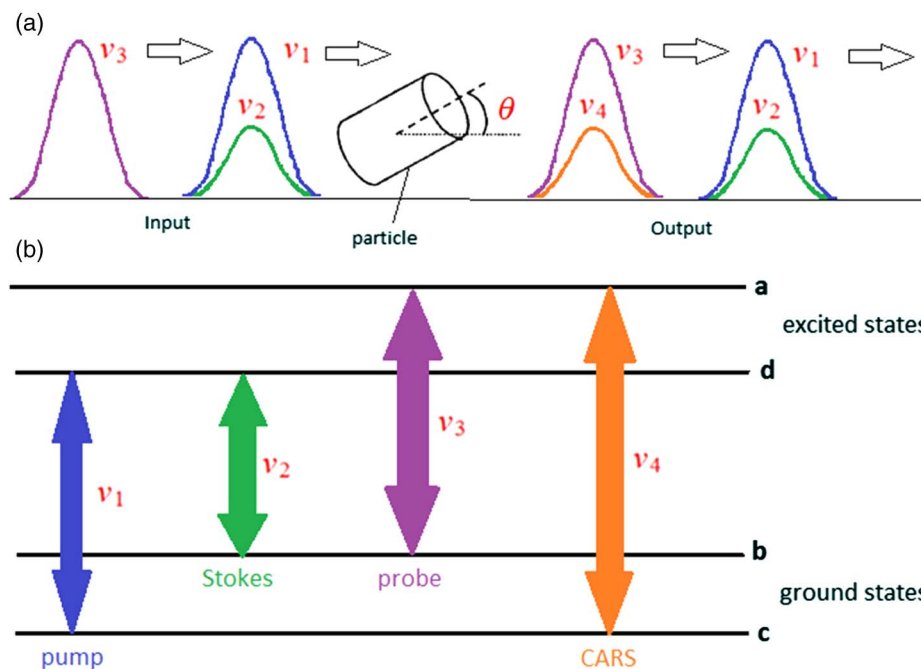
Fig. 1.   (a) FAST CARS configuration, which consists of preparation pulses v_1 and v_2 that provide the maximum coherence between ground vibrational states $|b\rangle$ and $|c\rangle$. Then, a time delayed probe pulse v_3 interacts with this oscillating molecular configuration to produce the anti-Stokes radiation as v_4. (b) Four-energy-level scheme of the system that describes the CARS process. v_1 and v_2 pulsed lasers involve transitions between ground states and excited level d, while v_3 and v_4 involve transitions between ground states and excited level a.

and nonlinear effects [20]. The correct pulse will stimulate a characteristic response of molecular vibrations. Once the optimized laser pulse configuration is acquired [21], the molecules in the ensemble are made to oscillate together due to induction by maximal coherence following probing in the UV region [22]. A couple of properly adjusted femtosecond laser pulses of the pump pulse with angular frequencies ω_p and a Stokes pulse, ω_s, will form a maximum Raman coherence $|\rho_{bc}|$ between the two molecular vibrational ground states, $|b\rangle$ and $|c\rangle$. Maximal coherence can be acquired through stimulated Raman adiabatic passage, where it is prepared by a counterintuitive pulse series [18]. A time-delayed probe field with higher frequency ω_{pr} will scatter this coherence off and will generate the coherently enhanced CARS signal at frequency $\omega_{CARS} = \omega_p - \omega_s + \omega_{pr}$. An intensity that is orders of magnitude more sensitive can be achieved. Pollution of fluorescence in resonance Raman spectra does not serve as a major obstacle, as eradication can be done by using pulses in the UV region. Enhancement of the signal will be compulsory, especially when a much weaker backward signal is engaged [23]. The CARS technique is experimentally practical, as an experiment has been done for bacterial spore detection in aqueous solution [24]. Its potential molecular characterization property may also provide new applications in the field of forensic science.

In this study, analysis of CARS of a single cylindrical particle is performed using semi-analytical result to comprehend the role of focused light on the angular dependence of CARS signal. Section 2 presents the formalism of the scattered CARS signal based on nonlinear scattering process with nonlinear polarization as a source. Gaussian beam approximation of the laser pulses is implemented to provide an analytical expression to the integral equation of the scattered signal field formulated. The analytical expression resides in the orientation factor term which includes polarizations of the lasers. Insights on the CARS scattering strength is found in the formulation of the intensity ratio and photon number ratio. The ratios are then compared with the derivations obtained from a relevant research of Pestov *et al.* [25]. The results are plotted and discussed in Section 3. In Section 4, the CARS signal is compared with reflection from perfect reflector disk to show the difference in the strength of the acquired signals and how it depends on the wavelength, particle size and detection scope.

Model of particle and level scheme: The particle is modeled in cylindrical coordinates as shown in Fig. 2(a) below. The spectroscopic fingerprints of the particles are reflected in the CARS signal with the application of adaptively engineered laser pulses. The scattered signal from the particle is evaluated at the observation point (R, Θ, Φ).

The internal energy of the particle is visualized as a four-level scheme as illustrated in Fig. 1(b). The four-level configuration is a satisfactory approximation taking into account that the preparation lasers and probe laser are close to resonant. The pump, Stokes, and probe laser beams are assumed to be collinear with each other. The electric dipole interaction dictates the laser interactions with the particle quantum mechanically. The time-delayed probe laser couples state a to b resonantly and scatters off the acquired coherence in order to generate a coherently strengthened CARS signal.

2. NONLINEAR SCATTERING FORMALISM

The theoretical derivations are the insights of this study that allow one to intuitively perceive the process of CARS. The detailed theory relevant to the CARS process is covered in this section. The derived formalism is utilized to comprehend the modifications of CARS spectra and signal intensity relative to laser parameters and the observation angle [26]. For a start,
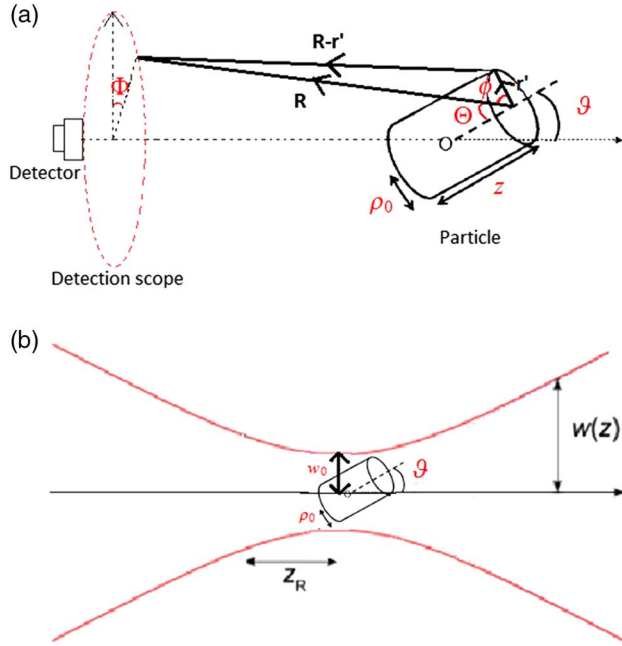
Fig. 2. (a) Graphical illustration of the system, where the single particle is modeled as a spherical particle. Measurement of the scattered signal field is performed by fixing the detector at one point. The CARS signal field E_4 is estimated at the observation point (R, Θ, Φ) generated from the particle into the detector. (b) Schematic drawing of particle specified in cylindrical coordinates with incident field lasers approximated as Gaussian beam.

the susceptibilities of the probe beam and the CARS signal are derived from the density matrix equations. Then an analytical solution to the integral equation of the scattered electric field signal outside the particle is presented. The heart of this study is the formulation of the orientation factor that bears the signatures of the CARS concept, which will then be reflected in two significant properties, which are the intensity ratio and the photon number ratio.

A. Scattered CARS Field

Analysis of a nonlinear medium with arbitrary geometry under the CARS scheme is performed. A particle subjected to preparation laser fields experiences nonlinear interactions as a response, producing third-order nonlinear polarization, P. Nonlinear polarization P functions as a source to yield the CARS signal $\tilde{\mathbf{E}}_4(\mathbf{R}, \omega)$, and it relies on the strength $E(t)$ of an applied optical field. The CARS signal is created from a four-wave mixing process due to the presence of third-order polarization. Coherent integration of the fields emanating from the dipoles covered by the volume V yields the scattered CARS signal in the far field. The dynamics during the application of the probe pulse and the generation of the anti-Stokes signal is governed by the density matrix equations [27]. The classical expression for the CARS field may be obtained from the solution of the inhomogeneous vector wave equation and was expressed in term of nonlinear susceptibility $\chi^{(3)}$ by Cheng *et al.* [8]. As in our previous work [28], our present study uses the quantum mechanical expression of the nonlinear polarization $\tilde{P}_p^{\mathrm{NL}}(\mathbf{r}', \omega) = \eta \mathcal{P}_{ca,p} \tilde{\rho}_{ac}^{(3)}(\mathbf{r}', \omega)$ to obtain the scattered CARS signal, which is complementary to the semiclassical approach of Cheng *et al.*. Here, $\tilde{\rho}_{ac}^{(3)}$ is the density matrix element that correlates with anti-Stokes emission, $\mathcal{P}_{ca,p}$ is

the dipole matrix element for the CARS transition, and η is number density. Appropriate engineered laser pulses will induce maximum ground state coherence. The density matrix equations are used to derive expressions for Raman coherence ρ_{bc} and anti-Stokes coherence $\rho_{ac}^{(3)}$. The density matrix element $\tilde{\rho}_{ac}^{(3)}(\mathbf{r}, \omega) = i\sum_{q,r,s} u_{3s}(\mathbf{r}) u_{2r}^*(\mathbf{r}) u_{1q}(\mathbf{r})(\mathcal{P}_{ab,s} E_{3s} \bar{\rho}_{bc}/\hbar (\gamma_{ac} - i\Delta_{ac}))$ can be obtained from the steady-state solution of density matrix equations with the assumption that polarization of the laser fields is along the x axis. The scattered CARS signal is expressed in cylindrical coordinates in terms of coherences as

$$\tilde{\mathbf{E}}_4(\mathbf{R}, \omega) = i \sum_{l,p=x\cdot y\cdot z} \hat{l}\, W_{lp} e^{ik_4(\omega)R} \frac{N\mu_0 \omega^2 \mathcal{P}_{ca,p}}{4\pi R}$$
$$\times \sum_{q,r,s} \frac{F_{qrs} \mathcal{P}_{ab,s} E_{3s}(t)}{\hbar(\gamma_{ac} - i\Delta_{ac})} \bar{\rho}_{bc}(0), \tag{1}$$

where $N = \eta V$ is the number of molecules and γ_{ac} is the decoherence rate of the transition that resulted in anti-Stokes emission, Δ_{ac} is the transition detuning, and $\bar{\rho}_{bc}(0)$ is the ground state coherence. The angular matrix element, which is described in Cartesian coordinates, is $W_{lp} = (\hat{\Theta} \cdot \hat{l})(\hat{\Theta} \cdot \hat{p}) + (\hat{\Phi} \cdot \hat{l})(\hat{\Phi} \cdot \hat{p})$, where the transformation unit vectors are $\hat{\Theta} = (\cos\Theta\cos\Phi, \cos\Theta\sin\Phi, -\sin\Theta)$ and $\hat{\Phi} = (-\sin\Phi, \cos\Phi, 0)$. The dimensionless geometrical and orientation factor F is

$$F_{qrs}(\Theta, \Phi, \omega) = \frac{1}{V} \int_0^{\rho_0} \rho\, d\rho \int_0^{2\pi} d\phi \int_0^l dz$$
$$\times u_{1,q}(\mathbf{r}) u_{2,r}^*(\mathbf{r}) u_{3,s}(\mathbf{r}) e^{-ik_4(\omega)\hat{R}\cdot\mathbf{r}}, \tag{2}$$

where $\hat{R} = (\sin\Theta\cos\Phi, \sin\Theta\sin\Phi, \cos\Theta)$ and $\mathbf{r} = (\rho\cos\varphi, \rho\sin\varphi\cos\vartheta - z\sin\vartheta, z\cos\vartheta + \rho\sin\varphi\sin\vartheta)$ is the position in the cylindrical microparticle tilted at an angle ϑ from the z axis. Thus

$$\hat{R} \cdot \mathbf{r} = \rho\sin\Theta(\cos\varphi\cos\Phi + \sin\varphi\cos\vartheta\sin\Phi)$$
$$+ z\cos\vartheta\cos\Theta + (\rho\sin\varphi\cos\Theta - z\sin\Theta\sin\Phi)\sin\vartheta. \tag{3}$$

The field dependent ρ_{bc} that gives rise to spatially dependent quantum coherence is neglected here. Thus, the quantum coherence directly affects the scattering through the orientation factor F in the cylindrical volume integration. The incident laser fields can be resolved into the spectral part and the spatial part. The spatial part is related to the incident laser beams by the expression $u_{j,g}(\mathbf{r}) = \tilde{E}_{j,g}/\tilde{E}_{j0}(\omega)$.

1. Gaussian Beam Approximation of Orientation Factor
The orientation factor F evolves from the integral equation of the scattered field. The pump, the Stokes, and the probe beam can be approximated as Gaussian beams in the paraxial approximation to simplify the electric field distributions for simulations. An analytical solution of the orientation factor can be obtained as a solution to the integral equation involving the Gaussian beams. The schematic diagram of the single particle in a Gaussian beam is shown in Fig. 2(b). The electric field vector of a Gaussian laser beam directed at an angle α from the z axis is

$$\tilde{\mathbf{E}}_j(\rho, \varphi, z) = \hat{u}_j E_{j0} \frac{w_{0j}}{w_j(z)} e^{\frac{-ik_j\rho^2}{2R_j(z)}} e^{-\frac{\rho^2}{w_j(z)^2}} e^{i\mathbf{k}_j \cdot \mathbf{r}} e^{i\varsigma_j(z)}$$

$$= (u_{jx}, u_{jy}, u_{jz}) E_{j0}, \tag{4}$$

where $j = 1, 2, 3$ is the laser index, with polarization unit vector $\hat{u} = (0, \cos\alpha, \sin\alpha)$ or $(1, 0, 0)$ for linear polarization and $\hat{u} = (1/\sqrt{2})(1, \pm i\cos\alpha, \pm i\sin\alpha)$ for circular polarization, with the wave vector $\mathbf{k} = k(0, \sin\alpha, \cos\alpha)$ and E_{j0} is the field strength at the focus, $z = 0$.

Here, w_0 is the beam waist, $w_j(z) = w_{0j}\sqrt{1 + (z/z_{Rj})^2}$ is the radius where the field amplitude and intensity fall to $1/e$ and $1/e^2$ from their axial values, $z_{R_j} = k_j w_{0j}^2/2$ is the Rayleigh range, $R_j(z) = z[1 + (z_{Rj}/z)^2]$ is the curvature radius of the wavefronts and $\varsigma(z) = \tan^{-1}(z/z_R)$ is the Gouy phase.

To obtain an insightful analytical expression, we assume the laser beam's axis and the cylinder's axis to be along the z axis by letting $\alpha = 0$. Furthermore, we assume that all the lasers have an identical shape and profile but with different frequencies and wave vectors. Thus, the general form of orientation factor F is expressed as

$$F_{qrs}(\Theta, \Phi, \omega) = e_{1,q} e_{2,r}^* e_{3,s} F(\Theta, \Phi, \omega), \tag{5}$$

where

$$F(\Theta, \Phi, \omega) = \frac{1}{V} \int_0^{\rho_0} \int_0^{2\pi} \int_0^l \left(\frac{w_0}{w(z)}\right)^3 \rho e^{-\rho^2 \left(\frac{3}{w(z)^2} + \frac{ik_{123}}{2R(z)}\right)} e^{i\varsigma(z)} e^{ik_{123}z}$$

$$\times e^{-ik_4[C\rho\cos(\phi-\eta) + z(\cos\vartheta\cos\Theta - \sin\Theta\sin\vartheta\sin\Phi)]} d\rho\, d\phi\, dz, \tag{6}$$

$$k_{123} = k_1 - k_2 + k_3, \tag{7}$$

$$C = \sqrt{\sin^2\Theta\cos^2\Phi + (\cos\vartheta\sin\Theta\sin\Phi + \sin\vartheta\cos\Theta)^2}, \tag{8}$$

$$\tan\eta = \frac{\cos\vartheta\sin\Theta\sin\Phi + \sin\vartheta\cos\Theta}{\sin\Theta\cos\Phi}. \tag{9}$$

2. Analytical Solution for Orientation Factor

The triple integral equation of F is reduced to acquire an analytical expression. Integration is performed analytically with respect to ϕ, yielding

$$F(\Theta, \omega) = \frac{2\pi}{V} \int_0^l \left(\frac{w_0}{w(z)}\right)^3 e^{i\varsigma(z)} \exp\{i\Delta k z\} H(z) dz, \tag{10}$$

where the phase mismatch depends on orientation and observation angles as

$$\Delta k = k_1 - k_2 + k_3 - k_4(\cos\vartheta\cos\Theta - \sin\Theta\sin\vartheta\sin\Phi). \tag{11}$$

The phase mismatch would be very small when $\cos\vartheta\cos\Theta - \sin\Theta\sin\vartheta\sin\Phi = 1$, particularly when Φ, ϑ, $\Theta = 0$.

The integral with respect to ρ is

$$H(z) = \int_0^{\rho_0} \exp\{-M\rho^2\} J_0(k_\Omega\rho) \rho\, d\rho, \tag{12}$$

$$M(z) = \frac{ik_{123}}{2R(z)} + \frac{3}{w(z)^2} = \frac{6z_R^2 + ik_{123}w_0^2 z}{2w_0^2(z_R^2 + z^2)}, \tag{13}$$

where $k_\Omega = k_4 C$ and J_0 is the Bessel function of the first kind. The key point in evaluating the integral equation is to approximate $J_0(k_\Omega\rho)$ by $\sin(k_\Omega\rho)/k_\Omega\rho$ as the lowest-order term. Integration with respect to ρ gives rise to the error functions that affect the shape of the angular dependence,

$$H(z) \simeq \frac{1}{k_\Omega} \int_0^{\rho_0} \exp\{-M\rho^2\} \sin(k_\Omega\rho) d\rho$$

$$\simeq \frac{i\sqrt{\pi}}{4k_\Omega\sqrt{M}} e^{-\frac{k_\Omega^2}{4M}} [-2\,\mathrm{erf}(G_0) + \mathrm{erf}(-G_-) + \mathrm{erf}(G_+)]. \tag{14}$$

The threefold integration is reduced further into a single fold integration. Then the analytical solution of F can be expressed as

$$F(\Theta, \omega)$$

$$\simeq \frac{z_R^3\sqrt{\pi^3}}{2iVk_\Omega} \int_0^l \frac{[2\,\mathrm{erf}(G_0) + \mathrm{erf}(G_-) - \mathrm{erf}(G_+)]}{\sqrt{M(z)}(z_R - iz)^2(z_R + iz)} e^{G_0^2} e^{i\varsigma(z)} e^{i\Delta k z} dz, \tag{15}$$

$$G_\pm(z) = \sqrt{M}\rho_0 \pm G_0, \qquad G_0(z) = \frac{ik_\Omega}{2\sqrt{M}}. \tag{16}$$

Note that for plane waves the Rayleigh range diverges, giving $(w_0/w(z)) \to 1$, $\varsigma, M \to 0$, $H \to (\rho_0/k_\Omega)J_1(k_\Omega\rho_0)$, and $F(\Theta, \omega) = (2\pi/V)(\rho_0/k_\Omega)J_1(k_\Omega\rho_0)(i/\Delta k)(1 - e^{i\Delta k l})$. These will be used to compare plane wave results with the results for Gaussian beams.

B. Analysis of Scattered CARS Signal

The analysis of the CARS signal is done through the intensity ratio and the photon number ratio. The intensity ratio is the ratio of the CARS signal intensity over the probe signal intensity, and the photon number ratio is defined as the ratio of the number of CARS photons over the number of probe photons. The ratios serve as measurements of the CARS signal strength. We obtain a more rigorous expression for the photon number ratio and compared it with the result of the CARS signal in the work of Pestov *et al.* [25].

1. Intensity Ratio

The intensity ratio measures the extent of the generated CARS signal. There have been few relevant studies of the intensity ratio and the ratio of signal photons over the number of incident photons [25,28]. The electric field is described as $E_{jg}(t) = E_{j0}p_{jg}$, where p_{jg} is the polarization components consisting of $p_{jx} = \sin a_j$, $p_{jy} = e^{ib_j}\cos a_j$, and $p_{jz} = 0$ for $j = 1, 2, 3$ and $g = p, q, r$, and s, assuming that the laser is traveling in the z direction and linearly polarized in the transverse component. The index p represents the anti-Stokes field,

s describes the probe field, and q and r denote the pump and Stokes fields, respectively. The Rabi frequencies are defined as $\Omega_j(\mathbf{r}, t) = (\sum_g u_{j,g}(\mathbf{r}) E_{j,g}(t) \mathcal{P}_{ak,g})/\hbar$. For $j = 1$ and 4, $k = c$; for $j = 2$ and 3, $k = b$. The scattered field is

$$\tilde{\mathbf{E}}_4(\mathbf{R}, \omega) = i \sum_{l,p=x\cdot y\cdot z} \hat{l} W_{lp} \mathcal{P}_{ca,p} \frac{e^{ik(\omega)R} N \mu_0 \omega^2}{4\pi R \hbar (\gamma_{ac} - i\Delta_{ac})}$$
$$\times F(\Theta) \sum_{q,r,s} \frac{\mathcal{P}^*_{r,db} \mathcal{P}_{q,dc}}{\mathcal{P}^2} E_{3s} \mathcal{P}_{ab,s} \bar{\rho}_{bc}(0), \qquad (17)$$

where $\sum_{q,r,s} (\sum_d \mathcal{P}^*_{r,db} \mathcal{P}_{q,dc})/\mathcal{P}^2$ corresponds to transitions from the ground state to excited state level d. The general form of the orientation factor has been replaced by the analytical one. The ground state coherence $\bar{\rho}_{bc}(0)$ is obtained as a steady-state solution to the density matrix equation, where it is expressed in the form

$$\bar{\rho}_{bc}(0) = \left(\frac{w_c^0}{\Gamma^*_{a'c}} + \frac{w_b^0}{\Gamma_{a'b}}\right) \frac{\Omega_1 \Omega_2^*}{(\Gamma_{bc} + \delta_S(t))}, \qquad (18)$$

where the Stark shift is $\delta_S(t) = (|\Omega_2(\mathbf{r}, t)|^2/\Gamma^*_{a'c}) + (|\Omega_1(\mathbf{r}, t)|^2/\Gamma_{a'b})$. The scattered field equation is rewritten as

$$\tilde{\mathbf{E}}_4(\mathbf{R}, \omega) = iE_{30} \sum_{l,p=x.y.z} \hat{l} W_{lp} \mathcal{P}_{ca,p} e^{ik(\omega)R}$$
$$\times \frac{\mu_0 \omega^2 N}{4\pi R \hbar \Gamma^*_{a'c}} F(\Theta) \bar{\rho}_{bc}(0)$$
$$\times \frac{1}{\mathcal{P}_{dc} \mathcal{P}^*_{db}} \sum_{qrs} p_{1q} \mathcal{P}_{ac,q} p^*_{2r} \mathcal{P}_{ab,r} p_{3s} \mathcal{P}_{ab,s}. \qquad (19)$$

Note that the components of the transition dipole moment satisfy the relations $|\mathcal{P}_{ab,x}|^2 = |\mathcal{P}_{ab,y}|^2 = |\mathcal{P}_{ab,z}|^2$ and $\mathcal{P}^2_{ab} = |\mathcal{P}_{ab,x}|^2 + |\mathcal{P}_{ab,y}|^2 + |\mathcal{P}_{ab,z}|^2 = 3|\mathcal{P}_{ab,x}|^2$ under statistical averaging. As the relation of the transition dipole moment and radiative decay is represented by $\mathcal{P}^2_{ab} = (3\hbar \varepsilon_0 \gamma_{\text{rad}} \lambda^3)/8\pi^2$, the average components for the transition dipole moment $\mathcal{P}_{ab}$ are $\mathcal{P}_{ab,x} = \mathcal{P}_{ab,y} = \mathcal{P}_{ab,z} = \sqrt{(\varepsilon_0 \hbar/8\pi^2)\lambda^3_{ab}\gamma_{\text{rad}}}$ and $\mathcal{P}_{ca,x} = \mathcal{P}_{ca,y} = \mathcal{P}_{ca,z} = \sqrt{(\varepsilon_0 \hbar/8\pi^2)\lambda^3_{ac}\gamma_{\text{rad}}}$, where γ_{rad} is the radiative decay rate of spontaneous emission from level a. Similarly, $\mathcal{P}^*_{db,x} = \sqrt{(\varepsilon_0 \hbar/8\pi^2)\lambda^{*3}_{db}\gamma'_{\text{rad}}}$ and $\mathcal{P}_{dc,x} = \sqrt{(\varepsilon_0 \hbar/8\pi^2)\lambda^3_{dc}\gamma'_{\text{rad}}}$, where γ'_{rad} is the radiative decay rate of spontaneous emission from level d. Eliminating the dipole moments, after lengthy derivations, yields the scattered CARS field as

$$\tilde{\mathbf{E}}_4(\mathbf{R}, \omega) = iE_{30} \begin{pmatrix} \sum_p W_{xp} \\ \sum_p W_{yp} \\ \sum_p W_{zp} \end{pmatrix} e^{ik(\omega)R} \frac{\mu_0 \omega^2 N}{4\pi R \hbar \Gamma^*_{a'c}}$$
$$\times \frac{1}{3} \frac{\hbar \varepsilon_0 \gamma_{\text{rad}} \sqrt{\lambda^3_{ca} \lambda^3_{ab}}}{8\pi^2} \frac{\sqrt{\lambda^3_{ca} \lambda^3_{ab}}}{\sqrt{\lambda^3_{dc} \lambda^3_{db}}}$$
$$\times F(\Theta) \bar{\rho}_{bc}(0) \sum_{qrs} p_{1q} p^*_{2r} p_{3s}. \qquad (20)$$

Signal intensity can be depicted as the square of the scattered CARS signal $I_4 = (cn\varepsilon_0/2)|\tilde{\mathbf{E}}_4(\mathbf{R}, \omega_{ac})|^2$, and the probe intensity is $I_3 = (cn\varepsilon_0/2)|\tilde{\mathbf{E}}_{30}(\omega_{ac})|^2$. Assuming an isotropic

medium, the general case for the intensity ratio is expressed as

$$\frac{I_4(\Theta, \Phi)}{I_3} = \left(\frac{1}{3} \frac{1}{8\pi} \frac{N}{\lambda_4^2 R}\right)^2 \frac{\lambda^3_{ca} \lambda^3_{ab} \gamma^2_{\text{rad}}}{(\gamma^2_{ac} + \Delta^2_{ac})} C(\Theta, \Phi)$$
$$\times |F(\Theta) \bar{\rho}_{bc}(0) P|^2 \frac{\lambda^3_{ca} \lambda^3_{ab}}{\lambda^3_{dc} \lambda^3_{db}} \qquad (21)$$

for $\mu_0 = 1/\varepsilon_0 c^2$ and $k = 2\pi/\lambda_4$, where $C(\Theta, \Phi) = (\sum_p W_{xp})^2 + (\sum_p W_{yp})^2 + (\sum_p W_{zp})^2$ and $P = \sum_{qrs} p_{1q} p^*_{2r} p_{3s}$.

2. Photon Number Ratio
Intensity can also be expressed in terms of the number of photons, which is $I = (\hbar \omega n / \tau A) = (2\pi \hbar c n / \lambda \tau A)$, where n is the number of photons, ω is the field frequency, λ is field wavelength, τ is the pulse duration, and A is the beam cross-sectional area. Thus, the photon number ratio is obtained from Eq. (21), giving

$$\frac{n_4}{n_3} = \frac{\tau_4 A_4}{\tau_3 A_3} \left(\frac{1}{3} \frac{1}{8\pi} \frac{N}{R}\right)^2 \frac{\lambda^3_{ca} \lambda^3_{ab} \gamma^2_{\text{rad}}}{\lambda^3_3 \lambda^3_4 (\gamma^2_{ac} + \Delta^2_{ac})}$$
$$\times C(\Theta, \Phi) |F(\Theta) \bar{\rho}_{bc}(0) P|^2 \frac{\lambda^3_{ca} \lambda^3_{ab}}{\lambda^3_{dc} \lambda^3_{db}}, \qquad (22)$$

A comparison is being made between the obtained photon number ratio and the result obtained from relevant research of Pestov *et al.* [25] In their work, the intensity ratio and the photon number ratio were derived from the study of the CARS signal generated from dipicolinic acid, DPA. The DPA serves as a marker for remote detection of bacterial spores. The intensity ratio was presented in the form of $(I_4/I_3)_{\text{PNAS}} = ((\pi N z |\bar{\rho}_{bc}|)/2\varepsilon_0 \hbar \lambda_4 V)^2 (\mathcal{P}^2_{ab} \mathcal{P}^2_{ac}/(\Delta^2 + \gamma^2_{ab}))$, while the photon number ratio was expressed as $(n_4/n_3)_{\text{PNAS}} = ((3/16\pi)(Nz/V)|\tilde{\rho}_{bc}|)^2 \lambda^3_{ab} \lambda^3_{ac} \gamma^2_{\text{rad}}/\lambda_3 \lambda_4 (\Delta^2 + \gamma^2_{ab})$, where V and z are the volume and length in Cartesian coordinates. Hence, the photon number ratio can be also expressed in terms of $(n_4/n_3)_{\text{PNAS}}$, which is of the form

$$\frac{n_4}{n_3} = \left(\frac{n_4}{n_3}\right)_{\text{PNAS}} \left(\frac{2}{9} \frac{V}{R \lambda_4 z}\right)^2 \frac{\tau_4 A_4}{\tau_3 A_3} C(\Theta, \Phi) |F(\Theta) P|^2 \frac{\lambda^3_{ac} \lambda^3_{ab}}{\lambda^3_{dc} \lambda^3_{db}}. \qquad (23)$$

The z dependence in Pestov's results appears because the scattered signal field is represented in Cartesian coordinates, while our study is performed using the cylindrical form. There are in fact few similarities between the number ratios formulated in this study and the number ratios presented by Pestov *et al.* The most notable difference is that their photon number ratio is inversely proportional to the signal wavelength λ_4, but our photon number ratio in Eq. (22) is inversely proportional to the cube of the signal wavelength λ_4. Pestov's expression did not possess the index d in the wavelength term as our expression does, where d indicates another excited level. If d is made equal to a, the wavelength term in our expression will reduce to a wavelength term similar to that in the expression of Pestov. If the size of the particle is much smaller than the probe beam cross-sectional area, the actual intensity should consider only the number of probe photons that impinge the particle. Then, energy conservation requires the photon number ratio to be less than unity, $(n_4/n_3) < 1$.

3. RESULTS AND DISCUSSION

The properties of the CARS signal are determined by the orientation factor, which is the key parameter that contains the products of the incident fields with the particle geometry, and it gives rise to the angular dependence of the CARS signal. The factor also contains the overlap between the linear response and the nonlinear process [26], which gives rise to the spectral variations with the observation angle. It was also found that particle size does not affect the notable spectroscopic peaks of CARS in the spectrum, but it does change the magnitude [29]. The focusing effect due to particle refraction is negligible for a particle with a size comparable to or smaller than the wavelength. Here, we focus on analyzing the angular dependence of the orientation factor, CARS intensity, and photon number ratios on the observation angle Θ for various laser and particle parameters.

Figures 3(a)–3(c) show the plots of orientation factor $|F|$ as a function of observation angle Θ for three different values of l. Numerical simulations of $|F|$ were performed by using the analytical orientation factor, Eq. (15). For small l [Fig. 3(a)], the $|F|$ does not show any oscillations, but has a minimum at around $\Theta = \pi/2$ and increases rapidly for the forward ($\Theta = 0$) and backward ($\Theta = \pi$) scatterings. For $l = 1$ μm, the magnitude of $|F|$ is largest at $\Theta = 0$, which is the forward scattering, as shown in Fig. 3(b). A similar trend is found in Figs. 3(a) and 3(c), which show that the magnitude increases as l decreases. The orientation factor $|F|$ affects the plot of intensity ratio I_4/I_3 and photon number ratio n_4/n_3 in Figs. 3(d)–3(f).

The pattern for $|F|$ looks quite identical to the ratios I_4/I_3 and n_4/n_3, although the magnitudes are different. This shows that the factor $C(\Theta, \Phi)$ in Eq. (21) has a very weak effect on the angular dependence. The magnitude for backward scattering is comparable with or slightly weaker than the magnitude

for forward scattering. A similar characteristic is found in previous work for spherical microparticle [28]. This means that utilization of the backward signal for detection purposes is as promising as the forward signal. The dip near $\Theta = \pi/2$ is due to destructive interference of the waves reflected from inner and outer boundaries, which are shifted out of phase. The pattern of the angular dependence changes with the values of l, showing a much smaller signal for larger l but with more rapid oscillations, showing a strong dependence on angle of observation Θ because of the larger phase mismatch for a longer cylindrical particle.

The photon number ratio as a function of observation angle and radius of particle ρ_0 is presented in Fig. 4 for three different values of l. The length and radius of cylindrical particle have significant effects on the number ratios through the orientation factor. The signal increases periodically (with oscillations) as ρ_0 becomes smaller and becomes larger for shorter cylinders (smaller l) because of good phase matching conditions. The CARS signal is strong around the forward and backward directions. For a circular disk geometry, small l, and large ρ_0, the intensity varies smoothly with no oscillations across Θ, and a minimum (dip) falls exactly at $\Theta = \pi/2$, as seen in Fig. 4(a).

All figures above are for $\vartheta = 0$. Figure 5 shows how the angular dependence of the CARS signal varies with the orientation angle of the cylinder ϑ. For $\vartheta = \pi/2$, the cylinder is oriented vertically while the detector goes around across a horizontal plane, and there is no angular dependence Θ. The number of lobes is reduced as the cylinder orientation changes from horizontal (along the z axis) to a vertical orientation. As the ratio l/ρ_0 increases, i.e., the cylinder becomes more elongated (disklike to rodlike), the oscillations across Θ become more rapid. The CARS signal is strongest when $\vartheta = 0$ in both forward and backward directions. It is interesting to see that at

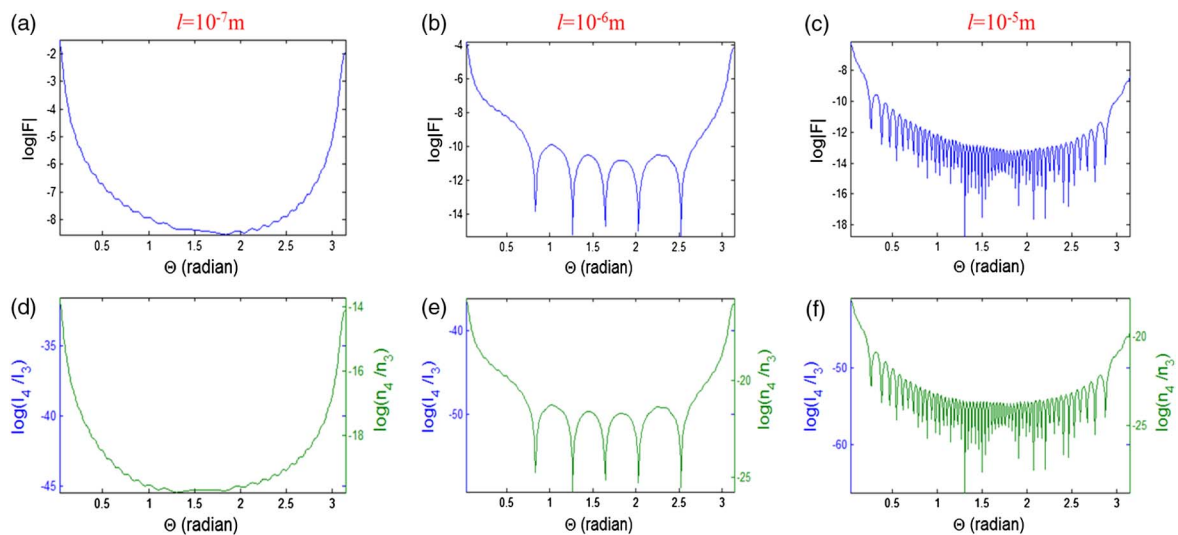Fig. 3.   Plot of $|F|$ as a function of observation angle Θ for three different l values: (a) $l = 10^{-7}$ m, (b) $l = 1$ μm, and (c) $l = 10^{-5}$ m. Plot of intensity ratio (log scale) $\log|I_4/I_3|$ (blue line) and log of photon number ratio $\log|(n_4/n_3)|$ (green line) versus Θ for (d) $l = 10^{-7}$ m, (e) $l = 1$ μm, and (f) $l = 10^{-5}$ m. We use $\Phi = 0$. The distance between detector and spore $R = 100$ m; the number of molecules $N = 5 \times 10^8$; radiative decay rate $\gamma_r = 108$ s^{-1}; decoherence rates $\gamma_{ac} = 2.5 \times 10^{12}$ s^{-1}, $\gamma_{ab} = \gamma_{ac}$, $\gamma_{bc} = 0.1 \times \gamma_{ac}$; detuning of the fields $\Delta_3 = 10^{12}$ s^{-1}, $\Delta_4 = \Delta_3$, $\Delta_2 - \Delta_1 = \delta = 0$; transition wavelengths $\lambda_{ab} = 380$ nm, $\lambda_{ac} = 370$ nm, $\lambda_{dc} = 1$ μm, and $\lambda_{db} = 1.01$ μm; wavelength of the probe field $\lambda_3 = \lambda_{ab}$; anti-Stokes wavelength $\lambda_4 = \lambda_{ac}$; particle radius $\rho_0 = 5$ μm; anti-Stokes wave vector $k = 2\pi/\lambda$; Rabi frequencies for pump beam are $\Omega_1 = 7\gamma_{ac}$ and for the Stokes beam are $\Omega_2 = 8\gamma_{ac}$; populations $\rho_{aa} = 0$, $\rho_{cc} = 0.9$, $\rho_{bb} = 1 - \rho_{aa} - \rho_{cc}$; beam waist radius $w_0 = 1.0\rho_0$; Rayleigh length $z_R = \pi w_0^2/\lambda$; polarization components $a_1 = a_2 = a_3 = \pi/4$ and $b_1 = b_2 = b_3 = \pi/2$; duration of the beams $\tau_3 = \tau_4$; and cross-sectional area $A_3 = A_4$. Here the cylinder is along the laser and z axis, i.e., $\vartheta = 0$.
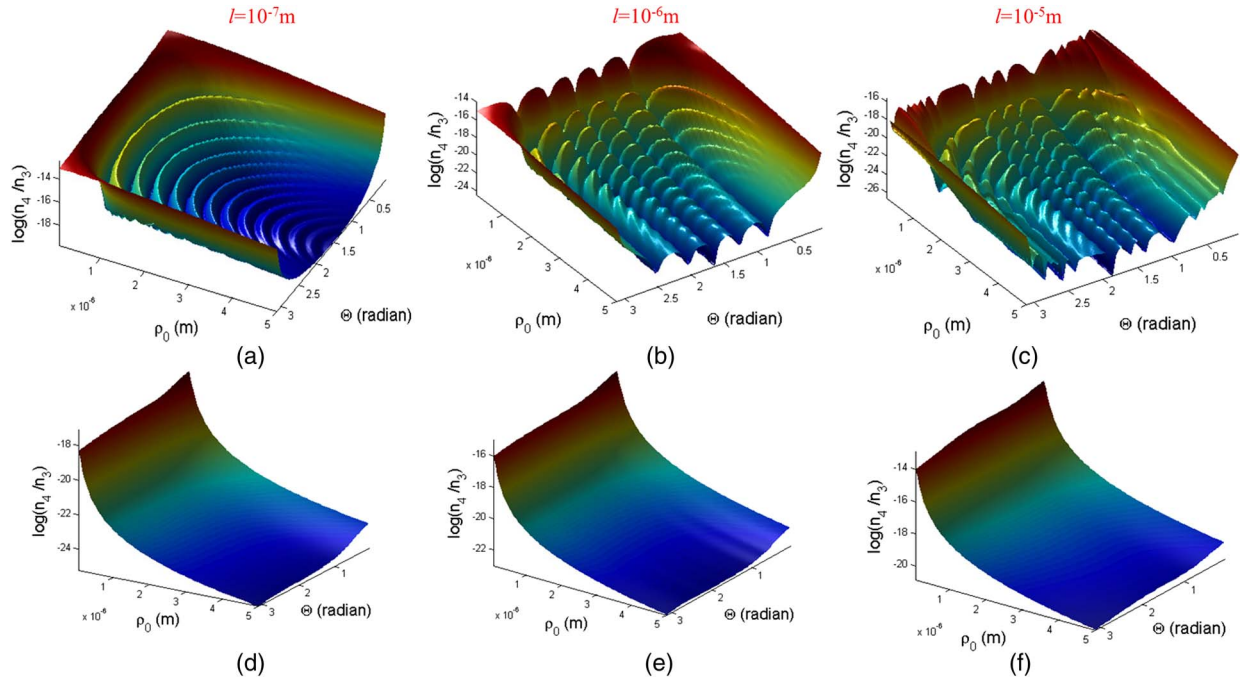
Fig. 4. 3D plot of log of photon number of CARS signal over probe photon number ratio $\log|(n_4/n_3)|$ as a function of angle of observation Θ and radius of particle ρ_0 for three values of l, which is the higher integral limit of the orientation factor $|F|$ with respect to z, for (a) $l = 10^{-7}$ m, (b) $l = 10^{-6}$ m, and (c) $l = 10^{-5}$ m. We use $w_0 = 5 \times 10^{-6}$ m for (a), (b), and (c) and $w_0 = 0.6\lambda/1.4\sqrt{2 \ln 2}$ for (d), (e), and (f), following [8]. Here, $\vartheta = 0$.
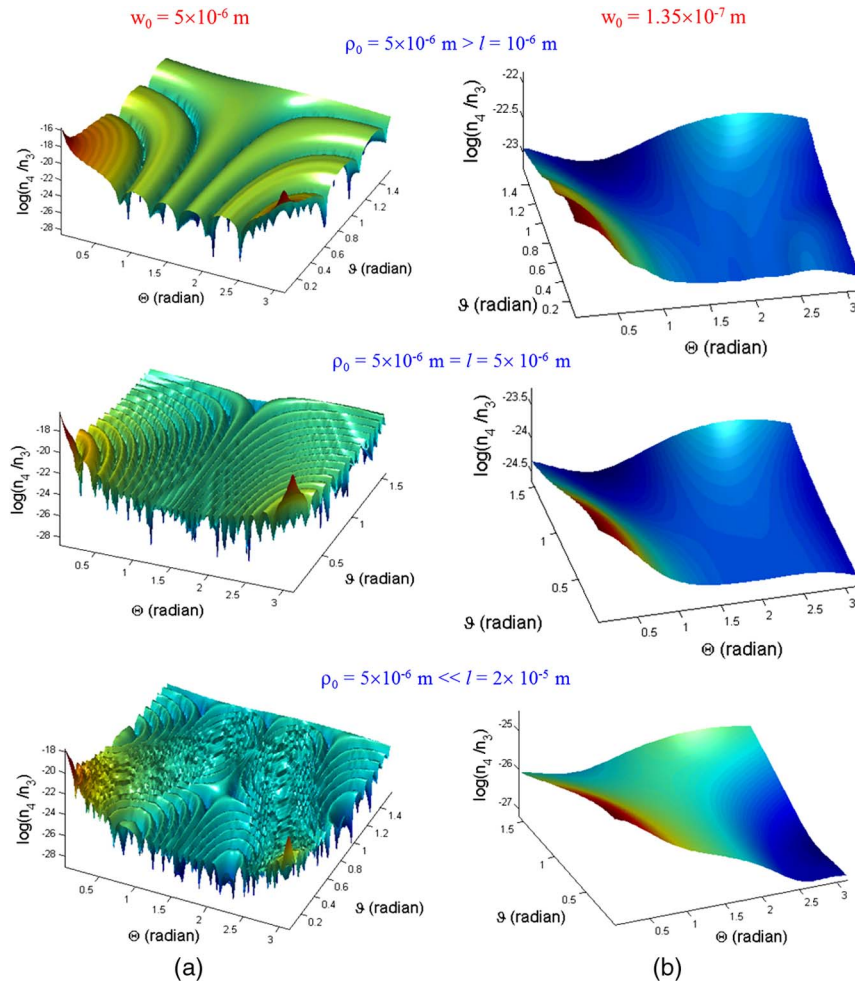

Fig. 5. Photon number ratio $\log|(n_4/n_3)|$ as a function of angle of observation Θ and cylindrical orientation angle ϑ for three scenarios of particle radius ρ_0 and length l: $\rho_0 > l$ (platelike), $\rho_0 > l$ and $\rho_0 < l$ (rodlike). We use (a) $w_0 = 5 \times 10^{-6}$ m and (b) $w_0 = 0.6\lambda/1.4\sqrt{2 \ln 2}$, following [8].

certain regular values of ϑ the forward and backward signals are extremely small, much smaller than other directions, as shown in Fig. 5(a). This implies that it may be harder to detect CARS signal from nonspherical microparticles.

When the waists of the lasers are reduced to $w_0 = 0.6\lambda/1.4\sqrt{2\ln 2}$ ($\simeq 0.135$ μm for $\lambda = 0.37$ μm) [8], Fig. 5(b) shows the disappearance of the oscillations. The CARS signal becomes much weaker, since the excited region in the particle is now smaller. The forward signal is much larger than the backward for $\vartheta = 0$. It is interesting to note that the trend reverses for $\vartheta = \pi/2$; the backward signal becomes larger. These features are almost independent of the ratio l/ρ_0, since the excitation dimension w_0 is smaller than l and ρ_0.

4. CONCLUSIONS

We have analyzed the emission properties of CARS signal from a cylindrical microparticle and found several new and significant results compared to the previous work [28]. At least two main new features in the present work are worth emphasizing.

First, we consider a cylindrical particle, which gives insight on how the CARS signal depends on the orientation with respect to the laser axis. There is no spherical symmetry as in the case of a spherical particle. The study of the nonlinear optical scattering for a cylindrical microparticle enables us to evaluate the scattering property in more realistic situations and covers more types of microparticles with a cylindrical geometry, especially biological samples such as bacteria. Unlike spherical microparticles, the present formalism enables us to study the optical response with respect to the orientation of the cylindrical particle.

Second, we use a Gaussian laser field instead of plane wave laser fields. This provides a realistic situation in the field of biophotonics involving nonlinear confocal microscopy and imaging of scattered light from microparticles excited by focused light with a high-numerical-aperture lens. We found that localized excitation by focused light gives rise to a different angular dependence. In particular the backward signal can be comparable or larger than forward for a cylindrical geometry when the cylinder is nearly vertical. This shows that in practice the much stronger forward signal is due to background, such as other four-wave mixing processes.

The combination of a cylindrical geometry with Gaussian focused beams enable us to obtain a semi-analytical expression of the orientation factor term that facilitates efficient and faster determination of the scattering intensity ratio, particularly the orientation factor, as the computation task has been reduced from threefold integrations to onefold integration.

Also, we have included the tensor property of the susceptibility, which was neglected in the previous paper [28], to obtain a scattering intensity ratio that is more rigorous and sensitive to laser polarizations. We compare the improved and generalized expression for the ratio with the expression in a previous paper [14].

To summarize, the strength of the CARS signal depends on the point of observation (particularly the angles Φ, Θ), particle radius ρ_0, its length l, and orientation ϑ. The acquired number of photons would eventually depend on the detection scope β. The semi-analytical expressions of the orientation factor, the intensity ratio, and the photon number ratio provide insights into the quantum nonlinear optical scattering properties of a cylindrical particle driven by focused lasers.

REFERENCES

1. D. Pestov, G. O. Ariunbold, X. Wang, R. K. Murawski, V. A. Sautenkov, A. V. Sokolov, and M. O. Scully, "Coherent versus incoherent Raman scattering: molecular coherence excitation and measurement," Opt. Lett. **32**, 1725–1727 (2007).
2. W. Demtroder, *Molecular Physics: Theoretical Principles and Experimental Methods* (Wiley-VCH, 2005).
3. H. Haken and H. C. Wolf, *Molecular Physics and Elements of Quantum Chemistry* (Springer-Verlag, 1995).
4. P. F. Chimento, M. Jurna, H. S. P. Bouwmans, E. T. Garbacik, L. Hartsuiker, C. Otto, J. L. Herek, and H. L. Offerhaus, "High-resolution narrowband CARS spectroscopy in the spectral fingerprint region," J. Raman Spectrosc. **40**, 1229–1233 (2009).
5. S. Rahav and S. Mukamel, "Stimulated coherent anti-Stokes Raman spectroscopy (CARS) resonances originate from double-slit interference of two-photon Stokes pathways," Proc. Natl. Acad. Sci. USA **107**, 4825–4829 (2010).
6. D. Oron, N. Dudovich, D. Yelin, and Y. Silberberg, "Quantum control of coherent anti-Stokes Raman processes," Phys. Rev. A **65**, 043408 (2002).
7. C. L. Evans and X. S. Xie, "Coherent anti-Stokes Raman scattering microscopy: chemical imaging for biology and medicine," Annu. Rev. Anal. Chem. **1**, 883–909 (2008).
8. J. X. Cheng, A. Volkmer, and X. S. Xie, "Theoretical and experimental characterization of coherent anti-Stokes Raman scattering microscopy," J. Opt. Soc. Am. B **19**, 1363–1375 (2002).
9. G. I. Petrov, R. Arora, V. V. Yakovlev, X. Wang, A. V. Sokolov, and M. O. Scully, "Comparison of coherent and spontaneous Raman microspectroscopies for noninvasive detection of single bacterial endospores," Proc. Natl. Acad. Sci. USA **104**, 7776–7779 (2007).
10. H. W. Wang, N. Chai, P. Wang, S. Hu, W. Dou, D. Umulis, L. V. Wang, M. Sturek, R. Lucht, and J. X. Cheng, "Label-free bond-selective imaging by listening to vibrationally excited molecules," Phys. Rev. Lett. **106**, 238106 (2011).
11. V. V. Yakovlev, H. F. Zhang, G. D. Noojin, M. L. Denton, R. J. Thomas, and M. O. Scully, "Stimulated Raman photoacoustic imaging," Proc. Natl. Acad. Sci. USA **107**, 20335–20339 (2010).
12. O. Katz, A. Natan, Y. Silberberg, and S. Rosenwaks, "Standoff detection of trace amounts of solids by nonlinear Raman spectroscopy using shaped femtosecond pulses," Appl. Phys. Lett. **92**, 171116 (2008).
13. N. G. Kalugin, L. Wang, Z. E. Sariyanni, Y. V. Rostovtsev, and M. O. Scully, "Multi-phonon absorption spectra of dipicolinic acid," Chem. Phys. Lett. **417**, 261–265 (2006).
14. D. Pestov, X. Wang, G. O. Ariunbold, R. K. Murawski, V. A. Sautenkov, A. Dogariu, A. V. Sokolov, and M. O. Scully, "Single-shot detection of bacterial endospores via coherent Raman spectroscopy," Proc. Natl. Acad. Sci. USA **105**, 422–427 (2008).
15. A. Dogariu, A. Goltsov, D. Pestov, A. V. Sokolov, and M. O. Scully, "Real-time detection of bacterial spores using coherent anti-Stokes Raman spectroscopy," J. Appl. Phys. **103**, 036103 (2008).
16. A. Portnov, I. Bar, and S. Rosenwaks, "Highly sensitive standoff detection of explosives via backward coherent anti-Stokes Raman scattering," Appl. Phys. B **98**, 529–535 (2010).
17. M. T. Bremer, P. J. Wrzesinski, N. Butcher, V. V. Lozovoy, and M. Dantus, "Highly selective standoff detection and imaging of trace chemicals in a complex background using single-beam coherent anti-Stokes Raman scattering," Appl. Phys. Lett. **99**, 101109 (2011).
18. V. A. Sautenkov, C. Y. Ye, Y. V. Rostovtsev, G. R. Welch, and M. O. Scully, "Enhancement of field generation via maximal atomic coherence prepared by fast adiabatic passage in Rb vapor," Phys. Rev. A **70**, 033406 (2004).

19. M. O. Scully, G. W. Kattawar, R. P. Lucht, T. Opatrny, H. Pilloff, A. Rebane, A. V. Sokolov, and M. S. Zubairy, "FAST CARS: engineering a laser spectroscopic technique for rapid identification of bacterial spores," Proc. Natl. Acad. Sci. USA **99**, 10994–11001 (2002).

20. H. Wang, D. Goorskey, and M. Xiao, "Enhanced Kerr nonlinearity via atomic coherence in a three-level atomic system," Phys. Rev. Lett. **87**, 073601 (2001).

21. D. Pestov, R. K. Murawski, G. O. Ariunbold, X. Wang, M. Zhi, A. V. Sokolov, V. A. Sautenkov, Y. V. Rostovtsev, A. Dogariu, Y. Huang, and M. O. Scully, "Optimizing the laser-pulse configuration for coherent Raman spectroscopy," Science **316**, 265–268 (2007).

22. N. Dudovich, D. Oron, and Y. Silberberg, "Single-pulse coherently controlled nonlinear Raman spectroscopy and microscopy," Nature **418**, 512–514 (2002).

23. V. Kocharovsky, S. Cameron, K. Lehmann, R. Lucht, R. Miles, Y. Rostovtsev, W. Warren, G. R. Welch, and M. O. Scully, "Gain-swept superradiance applied to the stand-off detection of trace impurities in the atmosphere," Proc. Natl. Acad. Sci. USA **102**, 7806–7811 (2005).

24. G. Petrov, V. Yakovlev, A. Sokolov, and M. Scully, "Detection of Bacillus subtilis spores in water by means of broadband coherent anti-Stokes Raman spectroscopy," Opt. Express **13**, 9537–9542 (2005).

25. D. Pestov, M. Zhi, Z. E. Sariyanni, N. G. Kalugin, A. A. Kolomenskii, R. Murawski, G. G. Paulus, V. A. Sautenkov, H. Schuessler, A. V. Sokolov, G. R. Welch, Y. V. Rostovtsev, T. Siebert, D. A. Akimov, S. Graefe, W. Kiefer, and M. O. Scully, "Visible and UV coherent Raman spectroscopy of dipicolinic acid," Proc. Natl. Acad. Sci. USA **102**, 14976–14981 (2005).

26. C. H. Raymond Ooi, "Theory of coherent anti-Stokes Raman scattering for mesoscopic particle with complex molecules: angular-dependent spectrum," J. Raman Spectrosc. **40**, 714–725 (2009).

27. D. R. Richardson, R. P. Lucht, W. D. Kulatilaka, S. Roy, and J. R. Gord, "Theoretical modeling of single-laser-shot, chirped-probe-pulse femtosecond coherent anti-Stokes Raman scattering thermometry," Appl. Phys. B **104**, 699–714 (2011).

28. C. H. Raymond Ooi, G. Beadie, G. W. Kattawar, J. F. Reintjes, Y. Rostovtsev, M. S. Zubairy, and M. O. Scully, "Theory of femtosecond coherent anti-Stokes Raman backscattering enhanced by quantum coherence for standoff detection of bacterial spores," Phys. Rev. A **72**, 023807 (2005).

29. C. H. Raymond Ooi, "Near-field and particle size effects in coherent Raman scattering," Prog. Electromagn. Res. **117**, 479–494 (2011).